

AI-Assisted Fusion of Scanning Electrochemical Microscopy Images Using Novel Soft Probe

Yi-Hong Lin, Chih-Ning Tsai, Po-Feng Chen, Yen-Tzu Lin, Sorour Darvishi, Hubert H. Girault, Tung-Yi Lin, Mei-Yi Liao, and Tzu-En Lin*



Cite This: *ACS Meas. Sci. Au* 2022, 2, 576–583



Read Online

ACCESS |



Metrics & More



Article Recommendations

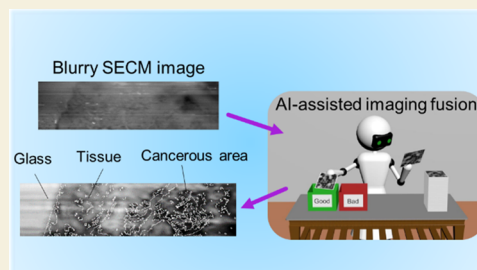


Supporting Information

ABSTRACT: Scanning electrochemical microscopy (SECM) is one of the scanning probe techniques that has attracted considerable attention because of its ability to interrogate surface morphology or electrochemical reactivity. However, the quality of SECM images generally depends on the sizes of the electrodes and many uncontrollable factors. Furthermore, manipulating fragile glass ultramicroelectrodes and blurred images sometimes frustrate researchers. To overcome the challenges of modern SECM, we developed novel soft gold probes and then established the AI-assisted methodology for image fusion. A novel gold microelectrode probe with high softness was developed to scan fragile samples. The distribution of EGFR (protein biomarker) in oral cancer was investigated.

Then, we fused the optical microscopic and SECM images to enhance the image quality using Matlab software. However, thousands of fused images were generated by changing the parameters for image fusion, which is annoying for researchers. Thus, a deep learning model was built to select the best-fused images according to the contrast and clarity of the fused images. Therefore, the quality of the SECM images was improved using a novel soft probe and combining the image fusion technique. In the future, a new scanning probe with AI-assisted fused SECM image processing may be interpreted more precisely and contribute to the early detection of cancers.

KEYWORDS: scanning electrochemical microscopy, SECM, gold soft ultramicroelectrode, oral cancer, EGFR, image fusion, artificial intelligence



1. INTRODUCTION

Oral cancer causes more than 300 000 new cases and over 140'000 deaths every year globally.¹ It can be classified into several subtypes, including malignant tumors in the oral cavity, malignant tumors in the lips, and the oropharynx.² Therefore, capturing oral cancer images to understand the cancer progression and its biomarker distribution is an important issue. In recent years, various scanning probe techniques have attracted considerable attention, such as electrochemical microscopy (SECM), scanning ion conductance microscopy (SICM), and atomic force microscopy (AFM).^{3–7} Moreover, scanning probe techniques combined with optical images can offer more information that allows scientists to understand chemical reactions during the catalytic processes and kinetics of certain chemical reactions.^{8–16} However, the quality of SECM images usually depends on the electrode sizes of the electrodes and many uncontrollable factors.^{17–22} For example, manipulating fragile glass ultramicroelectrodes and blurred images sometimes frustrates researchers.²³ Usually, scientists tend to fabricate smaller electrode probes to achieve better resolution, but the image speed will be slower and the fabrication processes are tedious.^{24,25}

To overcome the challenges of modern SECM, we improved electrochemical imaging using novel soft probes scanned in

contact mode and then established algorithm-assisted artificial intelligence (AI) for image fusion.^{26,27} First, we developed new ultrathin gold wire electrodes with extreme flexibility. The probes were made of gold wire and sealed in parafilm and polyimide (PI) membranes. Subsequently, the oral cancer biomarkers EGFR protein in tumor slices were labeled with primary and secondary antibodies with horseradish oxidase (HRP). HRP catalyzed the oxidation reaction of ferrocenemethanol (FcMeOH) to FcMeOH⁺ in the presence of FcMeOH and H₂O₂. When the probe was scanned over the location of biomarkers, the currents would increase due to the reduction of FcMeOH⁺ on the electrode surface and thus, generating an SECM image according to the current recorded at different locations on the sample surface.²⁸ Subsequently, the electrochemical images were merged with optical microscopic images to improve the quality of the SECM images. The merged images have clear tissue boundaries and provide information

Received: May 30, 2022

Revised: August 1, 2022

Accepted: August 2, 2022

Published: August 19, 2022



on the distribution of cancer biomarkers in oral cancer from different human bodies.

However, when the parameters of the image fusion process were changed, thousands of fused images were generated, which was confusing and annoying to the researchers. Fortunately, emerging trends in AI have revolutionized how we think and provided wide scopes of applications in electrochemistry, imaging processing, and material science.^{29–32} Machines can be trained to interpret images similarly to our brains and analyze them much more thoroughly than humans. For example, deep learning is a rapidly evolving form of AI that uses deep convolutional neural network (CNN) algorithm to mimic the human brain and has been prominently used to identify facial features, text, and voice.^{33,34} The CNN-based algorithm has been used to classify the medical images in clinical treatment and teaching tasks (e.g., pneumonia).^{33,35} CNN automatically extracts the features of the pictures of the hidden network with raw-image input data. VGG16 model belongs to the CNN family. It has a superficial layer architecture, but in this case, it can provide higher accuracy in the data set, and it is suitable for small data sets that only contain a few thousand images.^{36–38} In this work, deep learning was used to select good-quality fused images from thousands of merged pictures. In the future, AI-assisted fused SECM images may be interpreted with greater value and contribute to the early detection of cancers.

2. MATERIALS AND METHODS

2.1. Materials

FcMeOH (>95%) was purchased from Tokyo Chemical Industry, Japan. Monopotassium phosphate (KH_2PO_4 , 99.5%) and sodium chloride (NaCl , 99.5%) were purchased from SHOWA, Japan. Disodium phosphate (Na_2HPO_4 , 99%), monosodium phosphate (NaH_2PO_4 , 99%), hydrogen peroxide (H_2O_2 , pure, 30% w/w), and Tris base were purchased from Sigma-Aldrich. Anti-IL-6 antibody and goat anti-mouse IgG were bought from Abcam, UK. Bovine serum albumin (BSA) was purchased from Sigma-Aldrich. Xylene and Triton X-100 were purchased from Fisher. Ethanol (99.5%) was purchased from ECHO. Tween 20 was bought from Merck, Germany. Human oral cancer tissue array (product number T271b), oral cancer tissue array (product number T273), and human oral cancer tissue slices (product numbers HuCAT481 and HuCAT503) were purchased from Biomax. Details of human oral cancer samples are presented in the Supporting Information (SI) Table S1, including the patients' age and sex of the pathology sites. Deionized water was obtained from Sartorius (18.2 $\text{M}\Omega\text{-cm}$). The conductive silver paint was bought from Pelco. Polyimide was purchased from Kapton (DuPont). Parafilm was purchased from Parafilm M (Merck, Germany). Gold wire (25 μm) was purchased from Tanaka Electronics, Singapore. Sylgard 184 A&B was bought from Uni-Onward, Taiwan.

2.2. Pretreatment of the Tissue Slices

The tumor samples we studied were obtained from female and male patients between 12 and 68 years old. Before scanning with SECM, formalin-fixed paraffin-embedded (FFPE) oral cancer tissue slices were soaked in xylene solution for 10 min to remove paraffin and then immersed in five concentrations of alcohol (100, 95, 90, 70, 30%) for 5 min, respectively. After rehydrating the tissue slices, they were placed in a beaker containing Tris buffer (10 mM, pH 8) and heated to 95 degrees to restore antigen activity in the tissues. 3% hydrogen peroxide was added to avoid interference from endogenous peroxidase. Then, BSA was added to block the nonspecific adsorption. Subsequently, the solution of primary antibodies against EGFR or IL-6 (100 times diluted in PBS) was added and incubated for 1 h at room temperature (RT) and washed three times with Triton X-100 and PBS by placing the tissue in the buffer for 5 min. Finally, the slices

were immersed in secondary antibodies—HRP (200 times diluted in PBS), incubated for 1 h at RT, and washed with Triton X-100 and PBS as in the previous step.^{11,39,40}

2.3. SECM Measurements and Imaging

The fabrication of the newly developed soft gold ultramicroelectrode was described in the SI-2. In brief, the novel gold soft ultramicroelectrode was composed of two PI layers, conductive gold wire and a parafilm layer in the central part. The tiny gold wire (diameter = 25 μm) was connected with silver-coated conductive wire with silver glue. Figures S2 and S3 show the excellent softness and flexibility of the soft gold ultramicroelectrode, as it could even be bent like a hairpin. For testing its quality, cyclic voltammetry (CV) experiment was performed in 2 mM of FcMeOH. A commercial SECM (Ametek) ran under VersaStudio software (Ametek) was used. All SECM experiments were performed in a three-electrode arrangement under RT using an Ag wire as quasi-reference (QRE) and a Pt wire as the counter electrode (CE). All potentials reported here are given versus the Ag QRE. Data sets were treated and analyzed using MIRA software (Gunther Wittstock, Carl von Ossietzky University of Oldenburg, Germany). We adopted the contact mode for the SECM imaging of the distribution of EGFR and IL-6 in tissue slices. The soft probe was slightly contacted with the sample surface during forwarding line scans and recorded the current values. A lift-off routine was used in VersaStudio software to perform the SECM images. The pretreated tissue samples were immersed in an electrolyte containing 2 mM FcMeOH, 1 mM H_2O_2 , and 50 mM PB, pH 5.5. The soft gold electrode was scanned at a speed of 35 $\mu\text{m/s}$. A voltage of -0.2 V was applied to reduce FcMeOH⁺ generated from HRP. The measurement delay interval is 0.1 s. First, we checked the cyclic voltammetry to ensure the quality of the soft microelectrode. The probe was scanned in the x direction (x -line scan) in contact mode to investigate the oral cancer tissues. Finally, the XY area mode was selected to image the sample and analyze the distribution of biomarkers.

2.4. Image Processing

2.4.1. MIRA for Image Processing. The raw data from the SECM experiments were processed by MIRA software. Different plot styles can be selected in the MIRA operation window. We clicked the “subsets” in the “data” to adjust the color code of the graph and then clicked “XLoadct” in the “tools” to select the color of the chart; we could also select “Modify” to remove the extreme value or background interference of the SECM image, and finally, in the “IDL image window”, the two-dimensional and three-dimensional images could be plotted at the same time, showing the current values of the x , y , and z -axes.

2.4.2. Matlab Software for Image Fusion and Image Processing. First, the SECM data of tissue scanning was plotted as an image processed by MIRA software. The same cancerous tissue was observed under an optical microscope. The Matlab software could read the optical microscopic image and convert it into a grayscale image. The edge of the optical microscopic image was enhanced by the edge detection function in Matlab. The detailed procedures are listed in the SI-4. Consequently, a “wfusing” function in Matlab was applied to merge the SECM and optical images. Different parameters were tested for image fusion. Finally, around 4000 merged images with different edge thresholds, brightness, and patterns were generated.

2.5. Convolutional Neural Network

After fusing SECM images and constructing a training data set, we used the CNN model to process image classification. CNN is a widely used model in image classification; it is a model that uses multiple filters as sliding windows that scan around to extract local features and construct a higher-level abstract concept. In other words, it collects a lot of different small patterns and maps them into the whole image to build feature maps. Some hidden features between data are therefore distilled in this process through these layer structures, which makes it powerful for spatial feature extraction. CNN is usually composed of several convolution layers and pooling layers. Convolution layers are a

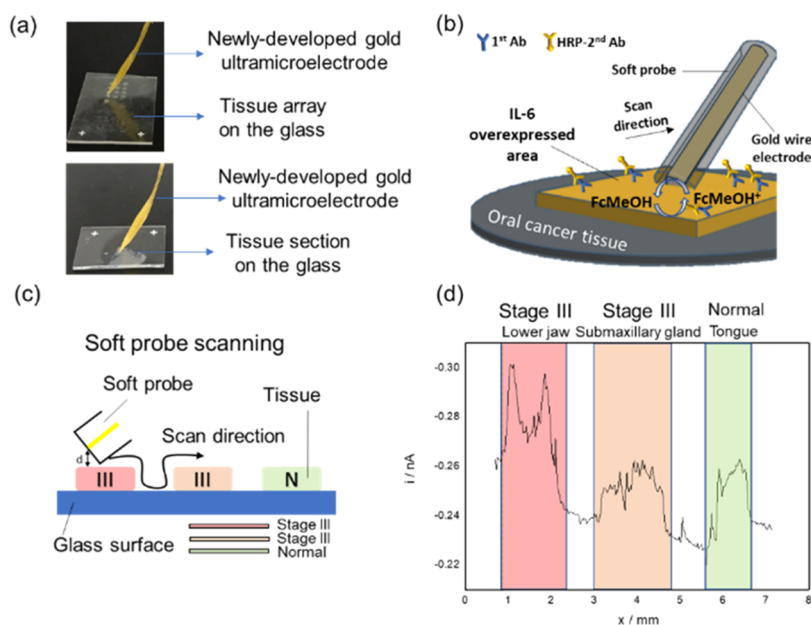


Figure 1. (a) Photos of the soft gold ultramicroelectrode scanned gently over the human oral cancer tissue biopsy array (upper picture) and the tissue section (lower picture) on the glasses in contact mode without damaging fragile samples. (b) Mechanism of SECM imaging of oral cancer biomarkers (e.g., IL-6). The rehydrated formaldehyde-fixed tissue was treated with primary and secondary HRP conjugated antibodies. The secondary HRP conjugated antibody in the tissue section catalyzed the oxidation of FcMeOH to FcMeOH⁺ in the presence of H₂O₂. (c) Schematic representation of the *x*-line scan from left to right in different IL-6-labeled oral tissue samples. (d) Scanning on *x*-line of different oral tissue samples.

series of filters that distill features as input for the next layers. As for the pooling layer, it is a downsampling method that comes with convolution layers. It reduces data dimensions by combining the outputs of neuron clusters at one layer into a single neuron and usually follows the convolution layers. Therefore, it can not only decrease the calculation cost and increase the generalization performance of the network but also accelerate the convergence speed of the model training.

CNN is commonly accompanied by fully connected layers and dropout layers. A fully connected layer, also called a dense layer, is the basic component of the neural network. It takes the features extracted by the convolution layers as input and maps them to the final output with some linear transformation. As for the dropout layer, it is a layer to prevent our model from overfitting, a phenomenon that the model considers the noise as a feature of the data by randomly setting some neurons to freeze with a certain possibility. To boost the image classification model, we reserved the original CNN model mentioned above and then appended VGG16, another model architecture, and used transferred learning to speed up the training time. The details of the AI model building can be found in the SI-5.

3. RESULTS AND DISCUSSION

In this work, a novel soft gold ultramicroelectrode was developed based on the widely used soft carbon stylus microelectrode (Ametek). The carbon paste part was replaced with 25 μm gold wire to enhance the stability of the probe. The problems of swelling and exfoliation of the carbon paste were solved. The 100 μm polyethylene terephthalate (PET) and the parylene C insulating layer were replaced with 5 μm PI film. Hence, the flexibility and practicality of the probe were greatly improved. Figure S2 and Figure S3 shows its advantages and extreme softness. Moreover, the fabrication process was much easier and less time-consuming, and the cost of the novel soft gold ultramicroelectrode was low. In the previous literature, we demonstrated the capability of a soft carbon stylus microelectrode for scanning various fragile and

rugged samples, for instance, melanoma tissues, without damaging the tip or sample. Therefore, we used the novel soft gold ultramicroelectrode developed in this work for further human tissue scanning experiments.

Figure 1a presents the photos of the soft gold ultramicroelectrode gently scanned on the human oral cancer tissue biopsy array and the tissue section on the glasses in contact mode without damaging fragile samples. Compared to conventional assays, such as fluorescent staining or immunohistochemistry (IHC), SECM can avoid optical interferences, including skin pigmentation and autofluorescence, to assist the clinical study of samples with a darker color or can be used along with other optical methods. To explore the biomarker distribution of human oral cancer samples from different people and different body parts while amplifying the signals of the target proteins, the biomarkers inside the tissue were labeled with the enzyme HRP. Figure 1b illustrates the mechanism of SECM imaging of oral cancer biomarkers. Rehydrated formaldehyde-fixed tissue was treated with primary and secondary HRP conjugated antibodies. The secondary HRP conjugated antibody in the tissue section catalyzed the oxidation of FcMeOH to FcMeOH⁺ in the presence of H₂O₂. We used the sample generation/ tip collection (SG/TC) mode and applied a constant voltage of -0.2 V at the ultramicroelectrode. The FcMeOH⁺ in the solution was reduced to FcMeOH on the electrode surface. Therefore, the more target molecules, the higher the current value was measured, and SECM could map the overexpressed areas.

After labeling IL-6 proteins, pretreated oral tissue samples from the tongue, mandible, and submandibular glands were scanned in the *x* direction with a soft gold probe. Figure 1c displays the SECM *x*-line scan of the tissue array containing normal tissue, stage I, II, and III oral cancer tissues. The current value was proportional to the quantity of biomarkers and therefore reflected the distribution of IL-6. The literature

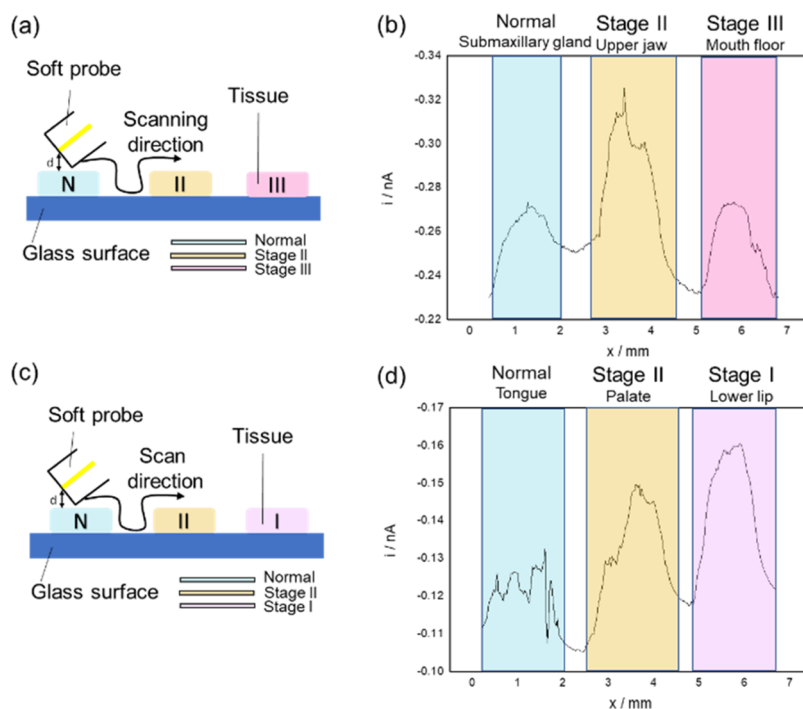


Figure 2. (a) Schematic representation of the x -line scan from left to right in different oral tissue samples labeled with EGFR antibody and HRP antibody. d is the distance between the sample and the probe. (b) x -Line scan plot of different EGFR-labeled oral tissue samples. (c) Schematic representation of the x -line scan from left to right in different EGFR-labeled oral tissue samples. d is the sample–probe distance. (d) X -Line scan plot of different oral tissue samples. Experimental conditions: WE = soft gold ultramicroelectrode, QRE = Ag wire, CE = Pt wire, $E = -0.2$ V, translation speed = $50 \mu\text{m/s}$, and delay of ADC time = 0.1 s.

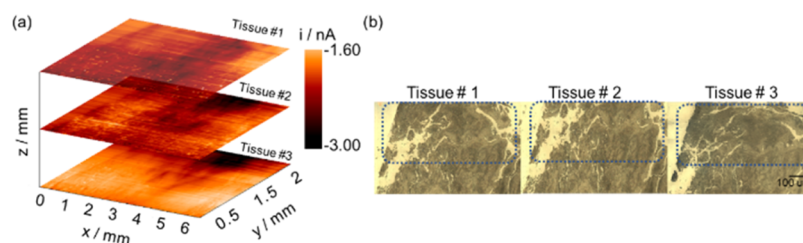


Figure 3. (a) Overlaid SECM images of oral cancerous tissue #1, tissue #2, and tissue #3 labeled with EGFR antibody and HRP secondary antibodies. (b) Optic microscopy images of oral tissue #1, tissue #2, and tissue #3. Experimental conditions: WE = soft gold ultramicroelectrode, QRE = Ag wire, CE = Pt wire, $E = -0.2$ V, translation speed = $50 \mu\text{m/s}$, and delay of ADC time = 0.1 s.

indicated that interleukin 6 (IL-6) is a potential biomarker for the oral cavity and oropharyngeal squamous cell carcinoma.⁴¹ In Figure 1d, the higher current value (more negative) over the lower jaw stage III oral cancer tissue indicated higher levels of IL-6 protein, while the current value of stage III oral cancer in the submandibular gland was slightly higher than that of normal tissue. To explore more facts about the distribution of IL-6 and compare the stability of the new gold ultramicroelectrode, we also investigated more SECM images and x -line scans using the carbon soft stylus microelectrode used in the previous study (Figure S10).¹¹ The sensitivity and quality of SECM images or line scans performed by the commercial soft carbon stylus electrode and the newly developed electrode were similar. The results of the line scan experiments were comparable.

After scanning several human oral cancer samples, we found that in some cases, the distribution and amount of IL-6 in stage I, II, and III oral cancer and normal tissues did not show obvious differences. The reasons for this phenomenon could be many. We inferred that IL-6 was involved in many

physiological and pathological processes, including Covid-19 infection, trauma, infection, inflammation, and the development of malignant tumors. Therefore, the expression level of IL-6 could be interfered with by many factors related to the patient's healthy state. Therefore, the accuracy was not high enough if we used IL-6 as the only biomarker to distinguish oral cancer and normal tissues. Therefore, we still require more evidence and samples to evaluate the precision of using the IL-6 protein as the only biomarker for oral cancer detection.

Since IL-6 overexpression could be found in many diseases, we investigated another biomarker, EGFR, to analyze with SECM.⁴² Pretreated human oral cancer samples were labeled with EGFR antibody and secondary antibody with HRP. Figure 2a,c illustrates the schematic representation of the x -line scan of different oral tissue samples using the soft probe. Figure 2b shows the normal submandibular glands labeled with the x -line scans of the EGFR antibody and the second-stage cancer tissues of the maxillary and third-stage cancer tissues of the floor of the mouth. Figure 2d presents the x -line scans of normal tongue tissue, second-stage cancer tissue of the upper

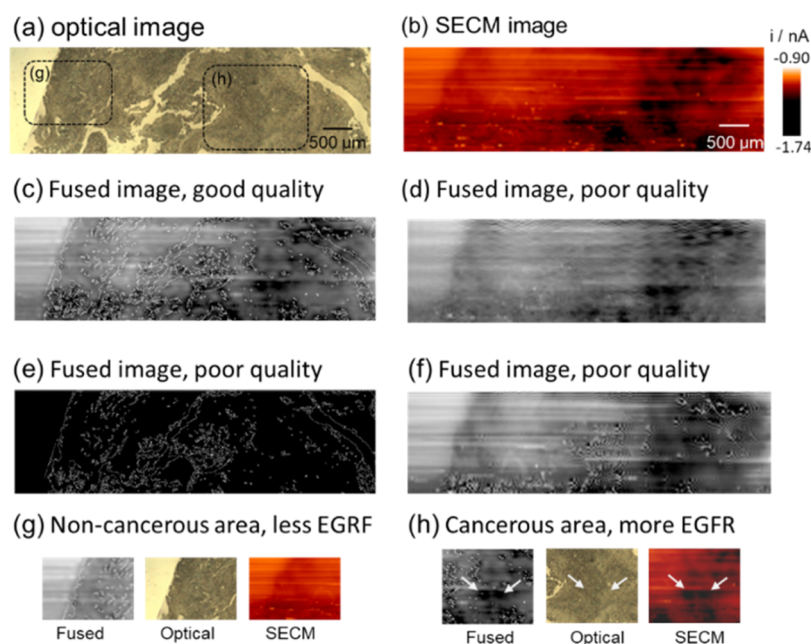


Figure 4. (a) Optical microscopic image of an oral cancer tissue section. (b) SECM images of an EGFR-labeled oral cancer tissue section. The darker parts revealed the presence of more EGFR in cancerous tissue. (c) Fused images with good quality. (d–f) Images fused with poor quality. (g) and (h) Enlarged pictures of noncancerous and cancerous areas of oral cancer tissue. The parts enlarged are labeled in panel (a).

jaw, and first-stage cancer tissue of the lower lip. Compared to normal tissues, the current values of cancer tissues were higher (more negative), representing more EGFR in cancer biopsies. Therefore, we speculate that EGFR is a better biomarker than IL-6 in these cases. However, the microelectrodes were fabricated manually, so it was difficult to compare the current values of different experiments. Also, although the sample–probe distance may be slightly different for each microelectrode, the trend of the x -line scan results was similar. In the x -line scans in Figures 1 and 2, the current value over the cancerous tissue was approximately 400 pA higher than that for normal tissues. Therefore, the slight variation of each microelectrode could cause some bias in the baseline, but it did not affect the results of the measurements.

For further investigation of the vertical and horizontal distribution of biomarkers in a tumor block, an EGFR-positive human oral cancer tumor was cut into three pieces with an interval of approximately 20 μm . These samples in the same tumor block were named tissue #1, tissue #2, and tissue #3. Figure 3a is the overlay of SECM images of tissue #1, tissue #2, and tissue #3. It reveals the three-dimensional (3D) distribution of EGFR in the tumor block. The higher current (darker parts) represented the locations of EGFR in the tumor. In Figure 3a, the features with darker color could be the cancerous area, which has higher amounts of EGFR. The microscopic pictures of tissue #1, tissue #2, and tissue #3 are displayed in Figure 3b. The scanned areas are roughly circled with dashed lines.

One of the advantages of the novel soft gold probe developed in this research is to minimize the side effect caused by topography interference. The soft gold microelectrode could scan the rigged sample surfaces in contact mode (Figure 2a,c). Therefore, the FcMeOH^+ generated from the HRP-antibody–EGFR complex could be mapped on the tissue surfaces. Although the thickness of the tissue was about 20 μm , the interference caused by the change in probe sample and topography was not obvious in Figure 3a. If the

topography could affect the current signals, the currents on the tissue surface would have been lower. On the contrary, the higher signals from HRP were detected on the tissue surface than on the glass surface in Figure 3a, suggesting that the effect of topography change could be ignored. As a result, SECM can be used as an imaging method that can uncover certain biomarkers, including IL-6 and EGFR. Meanwhile, it can avoid interferences such as sample color, sample roughness, and autofluorescence. However, when scanning with SECM, it is very difficult to locate the exact position of the area scanned on the sample. For example, the cancerous sites detected in Figure 3a could not be directly linked with their optical microscopic pictures displayed in Figure 3b. Moreover, the clarity of the SECM images was not as high as that of the optical microscopic pictures. Therefore, developing a methodology for integrating both SECM images and optical images could improve the resolution and quality of the images.

The quality and resolution of the electrochemical imaging depend on many factors, including the tip size, the reactivity of the target molecules, the convention of collecting the signals, the vibration interference, and the experience of the experiment operator. If we could fuse the SECM image with an optical microscopic image, the resolution and tissue boundary might be much clearer so that the distribution of biomarkers could be investigated more thoroughly. We used a built-in function in Matlab software for wavelet processing to process image fusion. This ready-made function, “wfsimg”, is widely used to merge two images, detect edges, or eliminate noise. The details of wfsimg are explained in the SI-4. Although it is a built-in function, there are a lot of parameters that should be adjusted in the fusion process, including (1) wavelets for processing image fusion; (2) wavelet processing decomposition level; and (3) aufsmeth and refuset, the methods for approximations and details, respectively. When these parameters are changed, details, edges, brightness, and features may greatly affect the quality of fused images.

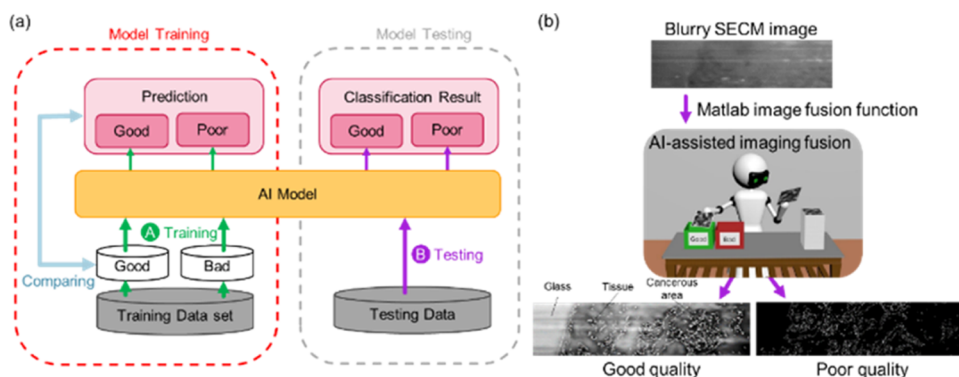


Figure 5. (a) Process of building the ML model. (b) AI-assisted image fusion can enhance the quality of the image, showing a clear tissue boundary and identifying the cancerous area (darker part).

We expect that the fusion process can extract the details and edge of the optical image and extract the features and brightness of the SECM image. Based on the Matlab official tutorial, several family wavelets (parameters) are included in the toolbox, such as Haar, Daubechies, Biorthogonal, and more tools. Each of them can yield different results from image fusion. Figure 4a shows the highly resolved optical microscopic image of oral cancer tissue, while Figure 4b presents an SECM image of the same oral cancer tissue. We have manually tried many combinations of the parameters for processing image fusion in Matlab. The fused images with good and poor qualities are presented in Figure 4c,d–f, respectively. Consequently, some merged images have the right brightness and boundary clarity, but some do not. In the good-quality fused image, Matlab software extracted the features of the tissue boundary in the optical microscopic picture (Figure 4a), resulting in the white frame in the fused image. The pale and dusky colors of the fused image are taken from the SECM image (Figure 4b). The darker parts represent the presence of EGFR, the biomarker secreted by cancer cells. The enlarged images of optical images, SECM images, and fused images are compared in Figure 4g,h. The areas corresponding to cancerous and noncancerous areas of Figure 4g, h are shown in Figure 4a. In Figure 4h, the exact cancerous area could be identified in an optical microscope after image fusion. The white arrows pointed out the cells with the highest level of EGFR expression in the fused image, which cannot be easily identified in the images that were not fused. However, trying all of the parameters for image fusion is impractical since one fusion process may generate more than 4000 fused images. Hence, we have to build a machine learning model that can be used to select the fused images with better quality.

After generating thousands of synthetic images, we expect the “artificial intelligence” to select the fused images with better quality, thus enhancing the significant features in the SECM images. To achieve this goal, we need to build an ML model and train it with many images to ‘learn’ how to distinguish images with good quality. Figure 5a shows the ML model building process. We chose one set of pictures to build the ML model. Around 4000 fused images generated by Matlab software were manually labeled as “good quality” and “poor quality”. Among them, 3000 images were used as training data, and 1000 images were used for testing. Subsequently, a famous ML model, the VGG16 model, was trained to classify the fused images. The VGG16 algorithm is a widely used CNN model that has been shown to perform well on a wide range of image classification tasks. The VGG16

model has 16 convolution layers, and each of them is followed by a maximum-pooling layer. After max pooling, the processed image representation is passed through three fully connected layers (FC) to predict the label (“good quality” or “poor quality”). Details of the model architecture and the training process can be found in the SI-5.

One of the indicators of evaluating the ML model is the accuracy of the classification of images with good or poor quality. After optimization, the proposed method using our model architecture was able to classify the SECM images well with very high accuracy of as high as 97%. Figure 5b shows the overall approach of AI-assisted image fusion to reveal cancerous areas according to biomarker distribution.

To further analyze the performance and effectiveness of AI models, four evaluation indicators were calculated after 500 fused pictures were classified. The four evaluation indicators include true positive (TP) numbers, false positive (FP) numbers, true negative (TN) numbers, and false negative (FN) numbers. TP stands for samples that are correctly classified as good quality. FP means that samples of poor quality are mistakenly classified as of good quality. TN represents those that are correctly classified as poor quality. FN is the number of samples that belong to good quality but are somehow classified as poor quality. Among these 500 pictures, the number of TP and TN was as high as 223 and 214. FP and FN were 2 and 12, respectively. These results indicated that the AI-assisted image classification tool was useful and practical. Since the “machine” can classify images as good quality and poor quality, researchers can apply this methodology to cope with blurred electrochemical images or apply this technique to bioimaging assays.

4. CONCLUSIONS

In conclusion, we have successfully developed super-soft gold ultramicroelectrodes to scan human oral cancer tissue sections and observe the biomarker distribution at different depths of the tumor. According to the experimental results, compared to the IL-6 protein, EGFR is a better oral cancer biomarker that can be used to distinguish cancerous tissues and normal tissues in the cases we studied. Moreover, we proposed a new AI-assisted methodology for processing SECM images by taking advantage of Matlab software, merging the optical and electrochemical images obtained from SECM. Images fused with different parameters were fed into our AI model to select the best images with the highest resolution, obvious cancer

boundary, and clear biomarker distribution among thousands of combinations, and the accuracy was 97%.

In addition, we expect to build a database of SECM images and microscopic images of different biomarker distribution in human tissues in the future. Automatic SECM experiments will be designed to distinguish the tumor border and stages of cancer while using the microfluidics-embedded soft gold electrode to instantly detect the biomarker and then release the cancer target drug to inhibit cancer cell division or induce cell apoptosis.

■ ASSOCIATED CONTENT

SI Supporting Information

The Supporting Information is available free of charge at <https://pubs.acs.org/doi/10.1021/acsmesuresciau.2c00032>.

Details of the experiments and soft gold microelectrode (PDF)

■ AUTHOR INFORMATION

Corresponding Author

Tzu-En Lin – Institute of Biomedical Engineering, Department of Electrical and Computer Engineering, National Yang Ming Chiao Tung University, 30010 Hsinchu, Taiwan; Present Address: No. 1001, Room 556B, Engineering Building 6, University Road, Institute of Biomedical Engineering, National Yang Ming Chiao Tung University, 30010 Hsinchu, Taiwan; orcid.org/0000-0003-4291-3601; Phone: +886-3-5731750; Email: telin@nycu.edu.tw

Authors

Yi-Hong Lin – Institute of Biomedical Engineering, Department of Electrical and Computer Engineering, National Yang Ming Chiao Tung University, 30010 Hsinchu, Taiwan

Chih-Ning Tsai – Institute of Biomedical Engineering, Department of Electrical and Computer Engineering, National Yang Ming Chiao Tung University, 30010 Hsinchu, Taiwan

Po-Feng Chen – Institute of Biomedical Engineering, Department of Electrical and Computer Engineering, National Yang Ming Chiao Tung University, 30010 Hsinchu, Taiwan

Yen-Tzu Lin – Institute of Biomedical Engineering, Department of Electrical and Computer Engineering, National Yang Ming Chiao Tung University, 30010 Hsinchu, Taiwan

Sorour Darvishi – Department of Chemistry and Chemical Engineering, École Polytechnique Fédérale de Lausanne (EPFL), CH-1950 Sion, Switzerland

Hubert H. Girault – Department of Chemistry and Chemical Engineering, École Polytechnique Fédérale de Lausanne (EPFL), CH-1950 Sion, Switzerland; orcid.org/0000-0001-5573-5774

Tung-Yi Lin – Institute of Traditional Medicine and Biomedical Industry Ph.D. Program, National Yang Ming Chiao Tung University, Taipei 11221, Taiwan

Mei-Yi Liao – Department of Applied Chemistry, National Pingtung University, Pingtung 90003, Taiwan; orcid.org/0000-0003-3872-0049

Complete contact information is available at: <https://pubs.acs.org/10.1021/acsmesuresciau.2c00032>

Author Contributions

The manuscript was written through the contributions of all authors. Conceptualization, T.-E.L.; validation, Y.-H.L., C.-N.T., P.-F.C., Y.-T.L., and S.D.; resources, T.-E.L., H.H.G., and T.-Y.L.; writing—original draft preparation, T.-E.L. and Y.-T.L.; writing—review and editing, H.H.G., T.-Y.L., M.-Y.L., and T.-E.L.; project administration, T.-E.L.; and funding acquisition, T.-E.L. All authors have read and agreed to the published version of the manuscript. Y.-H.L., C.-N.T., and P.-F.C. contributed equally to this work.

Funding

Ministry of Science and Technology (MOST) of Taiwan.

Notes

The authors declare no competing financial interest.

■ ACKNOWLEDGMENTS

T.-E.L. thanks the Young Scholar Fellowship Program of the Ministry of Science and Technology (MOST) in Taiwan, under Grant MOST 111-2636-E-A49-004- and the Higher Education Sprout Project of the National Yang Ming Chiao Tung University and the Ministry of Education, Taiwan. M.-Y.L. thanks MOST, under Grant MOST 110-2113-M-153-001-. Human protocols were consistent with national/international regulations and animal experiments, including the principles of replacement, reduction, and refinement. They were approved by the Research Ethics Committee for Human Subject Protection, National Yang Ming Chiao Tung University, Taiwan.

■ REFERENCES

- (1) Mustapha, A.; Mohamed, L.; Ali, K. An Overview of Gradient Descent Algorithm Optimization in Machine Learning: Application in the Ophthalmology Field. In *Communication in Computer and Information Science*, British Medical Journal Publishing Group, 2020; Vol. 1207, pp 349–359 DOI: [10.1007/978-3-030-45183-7_27](https://doi.org/10.1007/978-3-030-45183-7_27).
- (2) Montero, P. H.; Patel, S. G. Cancer of the Oral Cavity. In *Surgical Oncology Clinics of North America*, W.B. Saunders, 2015; pp 491–508 DOI: [10.1016/j.soc.2015.03.006](https://doi.org/10.1016/j.soc.2015.03.006).
- (3) Page, A.; Perry, D.; Unwin, P. R. Multifunctional Scanning Ion Conductance Microscopy. *Proc. R. Soc. A* **2017**, *473*, 20160889.
- (4) Preet, A.; Lin, T. E. A review: Scanning electrochemical microscopy (Secm) for visualizing the Real-Time Local Catalytic Activity. *Catalysts* **2021**, *11*, 594.
- (5) Izquierdo, J.; Knittel, P.; Kranz, C. Scanning Electrochemical Microscopy: An Analytical Perspective. *Anal. Bioanal. Chem.* **2018**, *410*, 307–324.
- (6) Eckhard, K.; Schuhmann, W. Alternating Current Techniques in Scanning Electrochemical Microscopy (AC-SECM). *Analyst* **2008**, *133*, 1486–1497.
- (7) Shi, X.; Qing, W.; Marhaba, T.; Zhang, W. Atomic Force Microscopy- Scanning Electrochemical Microscopy (AFM-SECM) for Nanoscale Topographical and Electrochemical Characterization: Principles. *Electrochim. Acta* **2020**, *332*, No. 135472.
- (8) Lin, Y.-T.; Darvishi, S.; Preet, A.; Huang, T.-Y.; Lin, S.-H.; Girault, H. H.; Wang, L.; Lin, T.-E. A Review: Electrochemical Biosensors for Oral Cancer. *Chemosensors* **2020**, *8*, 54.
- (9) Etienne, M.; Dossot, M.; Grausem, J.; Herzog, G. Combined Raman Microspectrometer and Shearforce Regulated SECM for Corrosion and Self-Healing Analysis. *Anal. Chem.* **2014**, *86*, 11203–11210.
- (10) Bondarenko, A.; Lin, T.-E. E.; Stupar, P.; Lesch, A.; Cortés-Salazar, F.; Girault, H. H.; Pick, H. Fixation and Permeabilization Approaches for Scanning Electrochemical Microscopy of Living Cells. *Anal. Chem.* **2016**, *88*, 11436–11443.

- (11) Lin, Y.-T.; Preet, A.; Chiu, Y.-P.; Yip, B.-S.; Girault, H. H.; Darvishi, S.; Wang, L.; Lin, T.-E. Communication- Scanning Electrochemical Microscopy Analysis of Interleukin-6 in Oral Cancer. *ECS J. Solid State Sci. Technol.* **2020**, *9*, No. 115028.
- (12) Alafeef, M.; Dighe, K.; Moitra, P.; Pan, D. Rapid, Ultrasensitive, and Quantitative Detection of SARS-CoV-2 Using Antisense Oligonucleotides Directed Electrochemical Biosensor Chip. *ACS Nano* **2020**, *14*, 17028–17045.
- (13) Teymourian, H.; Barfidokht, A.; Wang, J. Electrochemical Glucose Sensors in Diabetes Management: An Updated Review (2010-2020). *Chem. Soc. Rev.* **2020**, *49*, 7671–7709.
- (14) Elbadawi, M.; Ong, J. J.; Pollard, T. D.; Gaisford, S.; Basit, A. W. Additive Manufacturable Materials for Electrochemical Biosensor Electrodes. *Adv. Funct. Mater.* **2021**, *31*, No. 2006407.
- (15) Yang, Y. C.; Lin, Y. T.; Yu, J.; Chang, H. T.; Lu, T. Y.; Huang, T. Y.; Preet, A.; Hsu, Y. J.; Wang, L.; Lin, T. E. MXene Nanosheet-Based Microneedles for Monitoring Muscle Contraction and Electrostimulation Treatment. *ACS Appl. Nano Mater.* **2021**, *4*, 7917–7924.
- (16) Liu, D.; Li, W.; Zhu, C.; Li, Y.; Shen, X.; Li, L.; Yan, X.; You, T. Recent Progress on Electrochemical Biosensing of Aflatoxins: A review. *TrAC, Trends Anal. Chem.* **2020**, *133*, No. 115966.
- (17) Soldà, A.; Valenti, G.; Marcaccio, M.; Giorgio, M.; Pelicci, P. G.; Paolucci, F.; Rapino, S. Glucose and Lactate Miniaturized Biosensors for SECM- Based High-Spatial Resolution Analysis: A Comparative Study. *ACS Sens.* **2017**, *2*, 1310–1318.
- (18) Zhang, M.; Girault, H. H. SECM for Imaging and Detection of Latent Fingerprints. *Analyst* **2009**, *134*, 25–30.
- (19) Knittel, P.; Zhang, H.; Kranz, C.; Wallace, G. G.; Higgins, M. J. Probing the PEDOT: PSS/Cell Interface with Conductive Colloidal Probe AFM-SECM. *Nanoscale* **2016**, *8*, 4475–4481.
- (20) Kueng, A.; Kranz, C.; Lugstein, A.; Bertagnolli, E.; Mizaikoff, B. Integrated AFM-SECM in Tapping Mode: Simultaneous Topographical and Electrochemical Imaging of Enzyme Activity. *Angew. Chem., Int. Ed.* **2003**, *42*, 3238–3240.
- (21) Eckhard, K.; Schuhmann, W. Localised Visualisation of O₂ Consumption and H₂O₂ Formation by Means of SECM for the Characterisation of Fuel Cell Catalyst Activity. *Electrochim. Acta* **2007**, *53*, 1164–1169.
- (22) Kumar, S.; Sahoo, P. K.; Satpati, A. K. Electrochemical and SECM Investigation of MoS₂/GO and MoS₂/RGO Nanocomposite Materials for HER Electrocatalysis. *ACS Omega* **2017**, *2*, 7532–7545.
- (23) Kranz, C. Recent Advancements in Nanoelectrodes and Nanopipettes Used in Combined Scanning Electrochemical Microscopy Techniques. *Analyst* **2014**, *139*, 336–352.
- (24) Polcari, D.; Dauphin-Ducharme, P.; Mauzeroll, J. Scanning Electrochemical Microscopy: A Comprehensive Review of Experimental Parameters from 1989 to 2015. *Chem. Rev.* **2016**, *116*, 13234–13278.
- (25) Amatore, C.; Pebay, C.; Thouin, L.; Wang, A.; Warkocz, J. S. Difference between Ultramicroelectrodes and Microelectrodes: Influence of Natural Convection. *Anal. Chem.* **2010**, *82*, 6933–6939.
- (26) Lin, T.-E. E.; Lesch, A.; Li, C.-L. L.; Girault, H. H. Mapping the Antioxidant Activity of Apple Peels with Soft Probe Scanning Electrochemical Microscopy. *J. Electroanal. Chem.* **2017**, *786*, 120–128.
- (27) Wang, W. C.; Chung, H. H.; Dutkiewicz, E. P.; Wong, J. Y.; Yang, W. C.; Chang, C. L. T.; Hsu, C. C. On-site Diagnosis of Poultry Coccidiosis by a Miniature Mass Spectrometer and Machine Learning. *ACS Agric. Sci. Technol.* **2022**, *2*, 17–21.
- (28) Darvishi, S.; Pick, H.; Lin, T. E.; Zhu, Y.; Li, X.; Ho, P. C.; Girault, H. H.; Lesch, A. Tape stripping Electrochemical Detection of Melanoma. *Anal. Chem.* **2019**, *91*, 12900–12908.
- (29) Kaushik, A. K.; Dhau, J. S.; Gohel, H.; Mishra, Y. K.; Kateb, B.; Kim, N. Y.; Goswami, D. Y. Electrochemical SARS-CoV-2 Sensing at Point-of-Care and Artificial Intelligence for Intelligent COVID-19 Management. *ACS Appl. Bio Mater.* **2020**, *3*, 7306–7325.
- (30) Kakani, V.; Nguyen, V. H.; Kumar, B. P.; Kim, H.; Pasupuleti, V. R. A critical review on computer vision and artificial intelligence in food industry. *J. Agric. Food Res.* **2020**, *2*, No. 100033.
- (31) Gasteiger, J. Chemistry in Times of Artificial Intelligence. *ChemPhysChem* **2020**, *21*, 2233–2242.
- (32) de Almeida, A. F.; Moreira, R.; Rodrigues, T. Synthetic Organic Chemistry Driven by Artificial Intelligence. *Nat. Rev. Chem.* **2019**, *3*, 589–604.
- (33) Yadav, S. S.; Jadhav, S. M. Deep Convolutional Neural Network Based Medical Image Classification for Disease Diagnosis. *J. Big Data* **2019**, *6*, No. 113.
- (34) Rawat, W.; Wang, Z. Deep convolutional neural networks for image classification: A comprehensive review. *Neural Comput.* **2017**, *29*, 2352–2449.
- (35) Asgari Taghanaki, S.; Abhishek, K.; Cohen, J. P.; Cohen-Adad, J.; Hamarneh, G. *Artif. Intell. Rev.* **2021**, *54*, 137.
- (36) Ahmed, S.; Shaikh, A.; Alshahrani, H.; Alghamdi, A.; Alrizq, M.; Baber, J.; Bakhtyar, M. Transfer Learning Approach for Classification of Histopathology Whole Slide Images. *Sensors* **2021**, *21*, No. 5361.
- (37) Yang, H.; Ni, J.; Gao, J.; Han, Z.; Luan, T. A Novel Method for Peanut Variety Identification and Classification by Improved VGG16. *Sci. Rep.* **2021**, *11*, No. 15756.
- (38) Sony, S.; Dunphy, K.; Sadhu, A.; Capretz, M. A systematic review of convolutional neural network-based structural condition assessment techniques. *Eng. Struct.* **2021**, *226*, No. 111347.
- (39) Lin, T.-E. E.; Bondarenko, A.; Lesch, A.; Pick, H.; Cortés-Salazar, F.; Girault, H. H. Monitoring Tyrosinase Expression in Non-metastatic and Metastatic Melanoma Tissues by Scanning Electrochemical Microscopy. *Angew. Chem., Int. Ed.* **2016**, *55*, 3813.
- (40) Lin, T.-E.; Lu, Y.-J.; Sun, C.-L.; Pick, H.; Chen, J.-P.; Lesch, A.; Girault, H. H. Soft Electrochemical Probes for Mapping the Distribution of Biomarkers and Injected Nanomaterials in Animal and Human Tissues. *Angew. Chem., Int. Ed.* **2017**, *56*, 16498–16502.
- (41) st John, M. A. R.; Li, Y.; Zhou, X.; Denny, P.; Ho, C. M.; Montemagno, C.; Shi, W.; Qi, F.; Wu, B.; Sinha, U.; Jordan, R.; Wolinsky, L.; Park, N. H.; Liu, H.; Abemayor, E.; Wong, D. T. W. Interleukin 6 and Interleukin 8 as Potential Biomarkers for Oral Cavity and Oropharyngeal Squamous Cell Carcinoma. *Arch. Otolaryngol., Head Neck Surg.* **2004**, *130*, 929–935.
- (42) Weigum, S. E.; Floriano, P. N.; Christodoulides, N.; McDevitt, J. T. Cell-Based Sensor for Analysis of EGFR Biomarker Expression in Oral Cancer. *Lab Chip* **2007**, *7*, 995–1003.